Mineralogical Magazine (2023), **87**, 337–347
doi:10.1180/mgm.2023.18

CAMBRIDGE UNIVERSITY PRESS

Article

Quantitative evaluation of metamictisation of columbite-(Mn) from rare-element pegmatites using Raman spectroscopy

Yuanyuan Hao[1,2], Yonggang Feng[1,2], Ting Liang[1], Matthew Brzozowski[3], Minghui Ju[1], Ruili Zhou[1,2] and Yan Wang[4]

[1]School of Earth Science and Resources, Chang'an University, Xi'an, 710054, China; [2]Xi'an Key Laboratory for Mineralization and Efficient Utilization of Critical Metals, Chang'an University, Xi'an, 710054, China; [3]Department of Geology, Lakehead University, Thunder Bay, ON, P7B 5E1, Canada; and [4]Institute of Mineral Resources, Chinese Academy of Geological Sciences, Beijing, 100037, China

Abstract

Raman spectroscopic analysis was performed on columbite-(Mn) samples from a variety of previously studied rare-element pegmatites in Xinjiang, China, including the Jing'erquan No. 1 spodumene-subtype, Dakalasu No. 1 beryl–columbite-subtype and Kalu'an spodumene-subtype pegmatites, to quantify the relationship between the degree of metamictisation of columbite and Raman spectra. For all of the analysed columbites-(Mn), the position (p) and the full width at half maximum (FWHM) of the strongest band, A_{1g} vibration mode related to the Nb/Ta–O bond, in the Raman spectra have a negative correlation. Combined with previously determined U–Pb isotopic data and major–minor-element data for the columbites-(Mn), the degree of metamictisation was quantified using the alpha-decay dose (D) and displacement per atom (dpa), both of which were corrected for effects caused by annealing. The results demonstrate that the columbite-(Mn) from Jing'erquan and Kalu'an are very crystalline, whereas those from Dakalasu are transitional between crystalline and amorphous stages. The main factor influencing the key parameters, i.e. band position and FWHM, of the strongest Raman band of columbite-(Mn) is metamictisation caused by radiation damage, whereas composition and crystal orientation have limited influence. A set of equations are established to quantify the degree of metamictisation of columbite using the band position and the full width at half maximum: $FWHM = 8.309 \times \ln(^{a}D) + 30.11$ ($R^2 = 0.9861$); $p = -5.187 \times \ln(^{a}D) + 867.09$ ($R^2 = 0.966$); $FWHM = 8.1453 \times \ln(^{a}dpa) + 48.425$ ($R^2 = 0.9822$); and $p = -5.078 \times \ln(^{a}dpa) + 855.67$ ($R^2 = 0.9594$).

Keywords: columbite, metamictisation, Raman spectroscopy, α-dose, rare-element pegmatite

(Received 4 October 2022; accepted 7 March 2023; Accepted Manuscript published online: 17 March 2023; Associate Editor: Koichi Momma)

Introduction

Niobium and tantalum are critical metals that have been used increasingly in advanced technologies (e.g. information technology, energy, aerospace, national defence and military, Linnen *et al.*, 2012). Members of the columbite–tantalite solid-solution series are a major mineral resource of Nb and Ta, and have the formula, AB_2O_6, where A is occupied by Fe^{2+} and Mn^{2+} (Mg^{2+} in rare cases) and B is dominated by Nb^{5+} and Ta^{5+} (Černý and Ercit, 1989; Ercit, 1994; Romer *et al.*, 1996; Melcher *et al.*, 2015), and belong to the orthorhombic crystal system. There are three approved end-members in the columbite group: columbite-(Fe) [$Fe^{2+}Nb_2O_6$]; columbite-(Mg) [$Mg^{2+}Nb_2O_6$]; and columbite-(Mn) [$Mn^{2+}Nb_2O_6$]. In this paper the shortened form 'columbite' refers to all columbite end-members. This mineral group typically occurs in highly fractionated granites and granitic pegmatites (Linnen *et al.*, 2012; Feng *et al.*, 2019, 2020).

Corresponding author: Yonggang Feng; Email: ygfeng@chd.edu.cn
Cite this article: Hao Y., Feng Y., Liang T., Brzozowski M., Ju M., Zhou R. and Wang Y. (2023) Quantitative evaluation of metamictisation of columbite-(Mn) from rare-element pegmatites using Raman spectroscopy. *Mineralogical Magazine* **87**, 337–347. https://doi.org/10.1180/mgm.2023.18

In recent years, columbite has become an increasingly important mineral for U–Pb geochronology, and can provide robust age constraints for highly evolved granites and rare-element pegmatites (Romer and Smeds, 1994; Smith *et al.*, 2004; Baumgartner *et al.*, 2006; Melleton *et al.*, 2012; Deng *et al.*, 2013; Che *et al.*, 2015; Melcher *et al.*, 2017; Lupulescu *et al.*, 2018; Yan *et al.*, 2018; Zhou *et al.*, 2018; Feng *et al.*, 2019, 2020). However, analogous to zircon, the U–Pb isotopic ages of columbite are also discordant, and the principal reason is metamictisation. Although the metamictisation of zircon, the conventional mineral for age determination, has been studied intensely (Nasdala *et al.*, 2005, and references therein), that of columbite has received less interest (e.g. Lumpkin, 1998; Feng *et al.*, 2020).

Raman spectra reflect the inelastic Raman scattering of light that causes shifts in the frequency of the excitation laser. These frequency shifts depend solely on the inherent vibrational and rotational energy-level structure of the molecules interacting with the excitation laser. Different substances, therefore, have characteristic Raman spectra reflecting their unique molecular structures. Raman spectroscopy has many advantages, including small detection limits, simple sample preparation, and fast, economic, and non-destructive data acquisition (Nasdala *et al.*,

2004). It has been used widely for quantifying the degree of metamictisation of zircon in studies such as those of Nasdala *et al.* (1995), Zhang *et al.* (2000), Balan *et al.* (2001) and Nasdala *et al.* (2001b, 2004, 2005). These investigations demonstrated that the band position and full width at half maximum (FWHM) of a characteristic band of zircon [such as $\upsilon_3(SiO_4)$] changes systematically with the degree of metamictisation, and that this can be used to indicate quantitatively the degree of zircon metamictisation. At present, there are few Raman spectroscopy studies on columbite. Husson *et al.* (1977) analysed the Nb–O and M–O bonds of synthetic columbite-type niobates MNb_2O_6 (where M = Mg, Ca, Mn, Fe, Co, Ni, Cu, Zn and Cd). Moreira *et al.* (2010) conducted a systematic Raman spectroscopic study on a single, highly crystalline columbite-(Mn) crystal. Their results demonstrated that the Raman bands below 150 cm^{-1} and those at 250–380 cm^{-1} were related to A-site cations, whereas the other bands were more likely to be controlled by B–O bonds. The positions of strong Raman bands were influenced mainly by the presence of Nb and Ta in the B site (Husson *et al.*, 1977). Moreover, Moreira *et al.* (2010) demonstrated that the strongest band (A_{1g} vibration mode) occurred at ~882 cm^{-1}. Feng *et al.* (2020) conducted an integrated Raman spectroscopic, compositional, and U–Pb geochronological study on two columbite crystals from No. 1 pegmatite dyke at Dakalasu and discussed the relationship between metamictisation and age concordance. The relationship between metamictisation and Raman spectra, however, was not discussed.

In this contribution, we systematically investigated the Raman spectra of a representative suite of columbite samples from rare-element pegmatites in northwest China. The major–minor-element concentrations and U–Pb isotopic ratios of these samples were determined in a previous study (Feng *et al.*, 2019, 2020, 2021). The factors influencing the key parameters [i.e. position (p) and FWHM] of the strongest Raman band of columbites are explored, and the relationship between these parameters and the degree of metamictisation of columbite is discussed.

Previous studies have shown that, in common with zircon U–Pb isotopic ages, the U–Pb isotopic ages of columbite can also become discordant with metamictisation being one of the principal reasons (Romer, 2003; Feng *et al.*, 2019). Therefore, an in-depth understanding of the metamictisation of columbite is of considerable importance for the rational selection of analytical points, avoidance of invalid analyses and interpretation of columbite U–Pb isotopic ages obtained using *in situ* radiometric age determination techniques.

Sample descriptions

Six columbite samples were investigated in this study. Sample JR-1 was collected from the intermediate zone of the Jing'erquan No. 1 spodumene pegmatite located in the Eastern Tianshan, Xinjiang, China. Details of the regional and deposit geology are described by Yao *et al.* (2020), Liu *et al.* (2020) and Feng *et al.* (2021); information pertinent to this study are summarised below. This Li–Nb–Ta-mineralised pegmatite dyke occurs in the early Carboniferous Xiaorequanzi–Wutongwozi belts in the eastern section of the Quoltag Arc (Liu *et al.*, 2020). The ore minerals hosted by the pegmatite dyke mainly consist of spodumene, columbite-group minerals and lepidolite. Aggregates of green, scaly mica occur in the middle of the pegmatite and are associated with coarse-grained microcline. The grain size of columbite in sample JR-1 (Fig. 1) is in the range of 1–2 cm; it is associated mainly with spodumene, albite, quartz and phosphate minerals. The columbite-(Mn) is compositionally homogeneous, with an average #Mn [= molar Mn/(Mn + Fe)] of 0.84 and #Ta [= molar Ta/(Nb + Ta)] of 0.08 (Feng *et al.*, 2021). The U–Pb Concordia age obtained for this sample is 250.8 ± 1.0 Ma (Feng *et al.*, 2021).

Samples DKLS 107 and DKLS 108 were collected from the intermediate zone of the No. 1 pegmatite dyke at Dakalasu, which is located in the Altai orogenic belt, Xinjiang, China (Feng *et al.*, 2020). To date, the No. 1 pegmatite is the largest pegmatite dyke in the area and is characterised by significant Be, Nb, and Ta mineralisation. The pegmatite consists of a medium- to coarse-grained graphic texture zone and a megacrystic zone with miarolitic cavities (Wang *et al.*, 2003; Zou and Li, 2006). Both samples are single crystals several centimetres in size (Fig. 1). They are compositionally columbite-(Mn), with #Mn ratios of 0.79 and 0.72, and #Ta of 0.45 and 0.19, for DKLS 107 and DKLS 108, respectively (Feng *et al.*, 2020). The two samples have comparable #Mn ratios, but distinctly different #Ta, indicative of significant Nb–Ta fractionation and limited Fe–Mn fractionation (Feng *et al.*, 2020).

Samples K802 and K803 were collected from the intermediate zones of the 802 and 803 spodumene pegmatite dykes, respectively, of Kalu'an, which is located in the Kalu'an–Azubai pegmatite field in the Altai orogenic belt (Feng *et al.*, 2019). Exposed strata in the area are dominated by the Middle–Upper Silurian Kulumuti Group (Ma *et al.*, 2015). Both samples have been prepared as mounts of fine-grained mineral separates (>200 grains, Fig. 1) with the composition of columbite-(Mn). The #Mn ratios of the core, mantle and rim of individual grains in samples K802 and K803 are relatively constant, ranging from 0.90 to 0.95. The #Ta ratios of individual mineral grains, however, is highly variable. For sample K802, the average #Ta of the mantle of columbite grains (0.43) is notably higher than that of the core (0.14) and rim (0.20). Similarly, for sample K803, the average #Ta ratio of the Ta-rich mantle (0.49) is notably higher than that of the core (0.18), the Nb-rich mantle (0.18), and the rim (0.18) (Feng *et al.*, 2019).

Sample K650 is a mount comprising >200 columbite grains (Fig. 1) separated from the intermediate zone of the No. 650 pegmatite dyke of Kalu'an. The major-element compositions of these columbite grains were determined in the present investigation.

All of the separated columbite grains from each of the samples are columbite-(Mn). The compositional (electron microprobe) data of the columbite grains reported in previous studies (Feng *et al.*, 2019, 2020, 2021) are compiled in Supplementary Table S1.

Analytical methods

Back-scattered electron imaging and electron back-scatter diffraction

Back-scattered electron images were obtained using a FEI Quanta 650 Environmental Scanning Electron Microscope at the Xi'an Key Laboratory for Mineralization and Efficient Utilization of Critical Metals, Chang'an University to characterise the internal structure of columbite grains. The accelerating voltage was adjusted between 15–20 kV to optimise image quality. The spot size of the electron beam was 3.9 μm.

Electron back-scatter diffraction (EBSD) analysis of single-crystal samples JR-1, DKLS 107 and DKLS 108 was completed

https://doi.org/10.1180/mgm.2023.18 Published online by Cambridge University Press

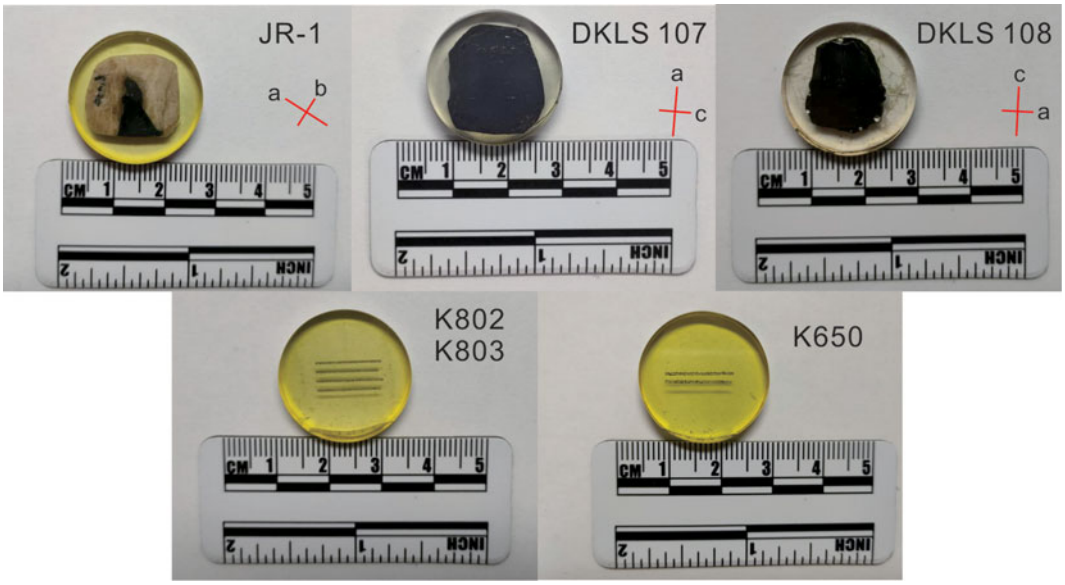

Figure 1. Photos of columbite samples from the investigated pegmatites: JR-1; DKLS 107; DKLS 108; K802 (the first two rows of grains); K803 (the two lower rows) and K650. In samples JR-1 to DKLS 108, 'a', 'b' and 'c' represent the long, middle and short axes of the crystals, respectively, which were determined using electron back-scatter diffraction [EBSD]).

at the State Key Laboratory of Continental Dynamics, Northwestern University using a FEI Quanta FEG 450 Field Emission Environmental Scanning Electron Microscope equipped with a Nordlys Nano electron back-scatter diffractometer produced by Oxford Instruments. The surface of the samples was polished prior to analysis. During analyses, the samples were inclined at 70° in the sample chamber, which was maintained under low vacuum (~40 Pa). The accelerating voltage was 20 kV and the beam spot size was 7.0 μm. Following the collection of a background signal, measurements were conducted on a series of spots from core to rim on individual columbite crystals to determine the orientation of the crystal lattice and obtain diffraction patterns. Calibration of the Kikuchi pattern was accomplished automatically using the instrument.

Major-element analysis

The major-element composition of columbite grains in sample K650 was determined at the Xi'an Key Laboratory for Mineralization and Efficient Utilization of Critical Metals, Chang'an University using a JEOL JXA-8100 electron microprobe (EPMA). The accelerating voltage and electron beam current were 15 kV and 20 nA, respectively. During EPMA, the peak counting time was 30 s for Sn and F, 10 s for W, Sc, Nb and Ta, and 15 s for Mn, Fe, Ca, Ti and Al. The compositions and formulae of the analysed columbite grains were calculated on the basis of six oxygen atoms. Details of the analytical parameters and the standards used for instrument calibration are summarised in Supplementary Table S2.

Raman spectroscopy

To characterise the relationship between metamictisation of columbite and their key Raman bands, the Raman spectra of the samples were determined at the Xi'an Key Laboratory for Mineralization and Efficient Utilization of Critical Metals, Chang'an University, using a LabRam HR evolution 800 mm confocal laser Raman spectrometer manufactured by HORIBA. The wavelength and energy of the excitation laser were set to 532 nm and 100 mW, respectively. The laser beam was focused on the sample surface through a 50× objective lens. A 100 μm pinhole and a 50% attenuation filter were used for controlling the signal intensity. A grating with a groove density of 600 grooves/mm was used for light dispersion. Spectra were acquired over a wavenumber range of 0–1200 cm^{-1} and represent the average of three accumulations of 28 s each. The *Labspec 6* software provided by HORIBA was used for baseline correction and smoothing of Raman spectra, calculation of band positions and FWHM values. Spectral resolution was ~1.2 cm^{-1}. Spectral fitting and correction for experimental band broadening used the method of Váczi and Tamás (2014).

Laser ablation inductively coupled plasma mass spectrometry

Laser ablation inductively coupled plasma mass spectrometry (LA–ICP–MS) U–Pb age determination of sample JR-1 was performed using a Thermo Fisher Scientific iCAP-Q model ICP–MS coupled to a RESOlution S155 193nm ArF excimer laser ablation system at the State Key Laboratory for Mineral Deposits Research, Nanjing University. The diameter of the laser beam was set to 43 μm. The laser output energy and repetition rate were 105 mJ and 4 Hz, respectively. Coltan 139 (with a reference age of 506.2 ± 5.0 Ma, Che *et al.*, 2015) was used as the external standard for calibrating U, Th and Pb isotopic ratios. Zircon standard samples 91500 and PL (Plešovice) were used as secondary standards to monitor U, Th and Pb isotope signals (Feng *et al.*, 2021). For each spot analysis, the signal of the gas background was collected for 20 s, followed by 50 s signal collection time on the standards or the unknown samples. The dwell time for ^{204}Pb, ^{206}Pb, and ^{208}Pb was 15 ms, for ^{207}Pb was 30 ms, for ^{232}Th and ^{238}U was 10 ms, and for ^{202}Hg was 6 ms. The concentrations of the rare earth elements (REE) were determined simultaneously

https://doi.org/10.1180/mgm.2023.18 Published online by Cambridge University Press

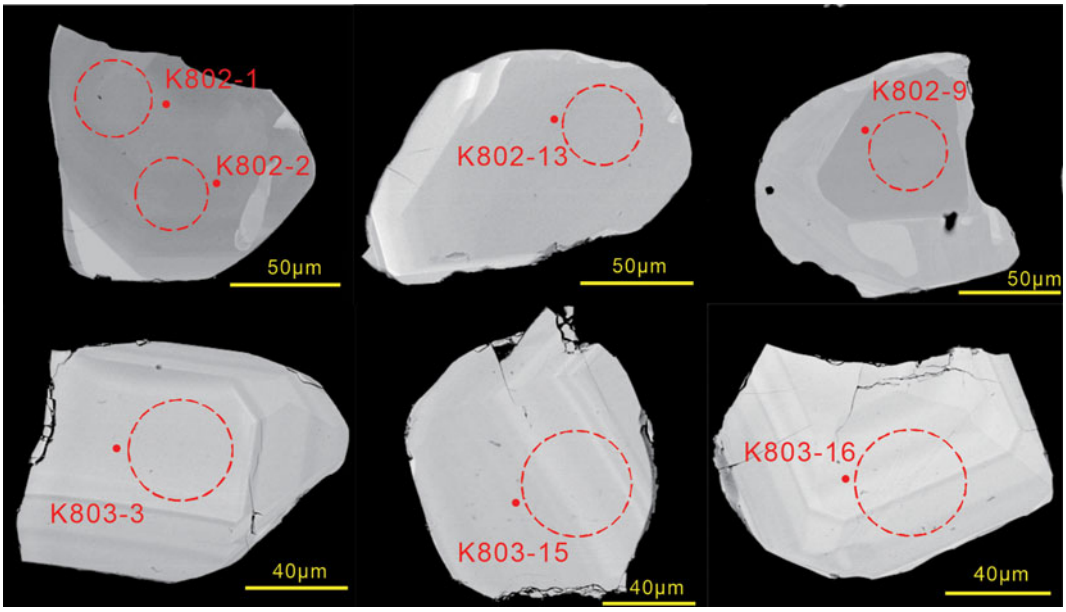

Figure 2. Representative back-scattered electron images of columbite in samples K802 and K803 from the Kalu'an pegmatite (modified after Feng *et al.*, 2019). The red dashed circles represent the location of laser ablation analyses, whereas the red solid dots indicate the position of electron microprobe and Raman spectroscopic analyses.

with U, Th and Pb. Each experiment consisted of the following sequence of analyses: one analysis of NIST SRM 610, two analyses of 91500, two analyses of Coltan 139, and one analysis of PL, followed by six sample analyses. For a detailed description of the analytical procedure, see Che *et al.* (2015). The $^{206}Pb/^{238}U$, $^{207}Pb/^{235}U$, $^{207}Pb/^{206}Pb$ and $^{208}Pb/^{232}Th$ ratios and U–Pb radiometric age were calibrated using *Iolite v3.7* (Hellstrom *et al.*, 2008) and *Isoplot 3.0* (Ludwig, 2003). Due to the low common Pb (^{204}Pb) concentrations in the columbite samples, no correction was applied for common Pb.

Results

Electron back-scattered diffraction

Back-scattered electron (BSE) images of representative columbite grains in samples K802 and K803 are shown in Fig. 2. The BSE images illustrate that the columbite grains in sample K802 are compositionally zoned, with the core and rim generally coloured grey, and the mantle being relatively bright (e.g. K802-1, K802-2, K802-13 and K802-9 in Fig. 2). Compared to sample K802, columbite grains in sample K803 exhibit oscillatory zonation (e.g. K803-3, K803-15 and K803-16 in Fig. 2).

The crystallographic orientations of the coarse-grained columbite crystals in samples JR-1, DKLS 107, and DKLS 108 (Fig. 1) are illustrated in Fig. 3. The a, b and c axes represent the long, medium and short axis directions, respectively, corresponding to the a, b and c axes in Fig. 1.

Electron probe microanalysis

The compositional data from previous work on samples K802, K803, DKLS 107, DKLS 108 and JR-1 by Feng *et al.* (2019, 2020, 2021) are compiled in Supplementary Table S1. Twenty-eight analyses were acquired here for further analysis of columbite grains in sample K650. The analytical results are provided in Table 1. Columbite grains in this sample are compositionally columbite-(Mn). The grains are compositionally homogeneous, with no obvious change in element concentrations from core to rim.

Raman spectroscopy

Totals of 92, 20, 20, 38, 32 and 49 Raman spectra were acquired for columbite grains in samples JR-1, DKLS 107, DKLS 108, K802, K803 and K650, respectively. The strongest Raman band (i.e. the A_{1g} vibration mode related to the B–O bond) for columbite-(Mn) from the No. 1 pegmatite at Jing'erquan (JR-1) occurs at 866.5–872.7 cm^{-1}, with corresponding FWHM values of 21.1–30.2 cm^{-1}. The strongest Raman band for columbite-(Mn) from the No. 107 and No. 108 pegmatites at Dakalasu (DKLS 107 and DKLS 108) occur at 852.3–866.2 cm^{-1} and 854.1–864.8 cm^{-1}, respectively, with corresponding FWHM values of 26.5–54.1cm^{-1} and 32.7–50.7cm^{-1}. The strongest Raman band of columbite-(Mn) in the Kalu'an pegmatite (K802, K803 and K650) are 873.1–878.2 cm^{-1}, 870.1–877.9 cm^{-1} and 871.5–878.3 cm^{-1}, respectively, with corresponding FWHM values of 13.4–20.4 cm^{-1}, 13.4–26.3 cm^{-1} and 10.1–26.9 cm^{-1}, respectively. Details of the key parameters of the characteristic Raman bands in these samples are provided in Supplementary Table S3. Representative Raman spectra of columbite-(Mn) from each pegmatite are shown in Fig. 4, with information on their Raman characteristic band (band position and FWHM) provided in Table 2. The position and FWHM of the characteristic Raman band for the columbite-(Mn) grains have negative correlation (Fig. 5).

U–Pb geochronology

Feng *et al.* (2019, 2020, 2021) acquired the U–Pb radiometric ages of columbite grains for samples JR-1, DKLS 107, DKLS 108, K802, and K803; the U–Pb isotopic data are compiled in Supplementary

https://doi.org/10.1180/mgm.2023.18 Published online by Cambridge University Press

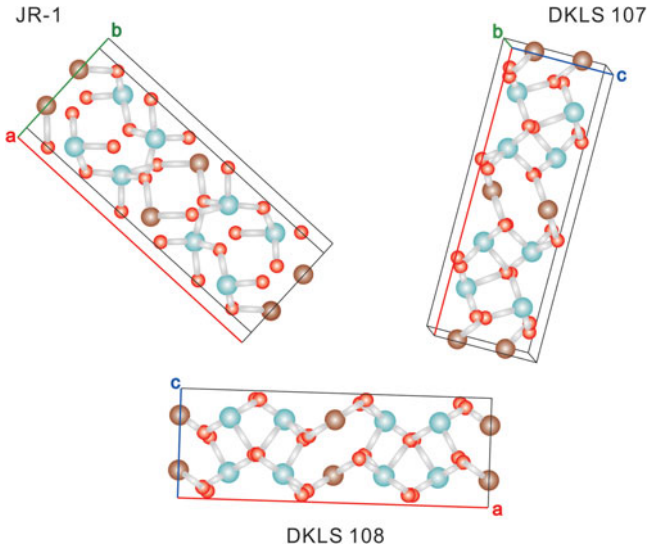

Figure 3. Crystallographic orientations of columbite grains in samples JR-1, DKLS 107 and DKLS 108 obtained using EBSD. The brown balls represent divalent cations of Fe and Mn in the A-site; the blue balls denote pentavalent cations Nb and Ta in the B-site; and the red balls represent O anions. The crystal structures of the columbite are modified after Tarantino and Zema (2005).

Table S4. An additional 39 analyses were collected here for further analysis for columbite-(Mn) sample JR-1 to establish a complete dataset including Raman spectra and columbite composition data. The spots analysed were distributed approximately evenly between the core, mantle and rim of the columbite-(Mn) grain in regions devoid of inclusions and fractures. Uranium–Th concentrations, isotope ratios, and ages are provided in Table 3. Average U and Th concentrations of 39 points are 1454.3 ± 279.0 ppm and 17.3 ± 5.6 ppm, respectively. The $^{206}Pb/^{238}U$ and $^{207}Pb/^{235}U$ ratios are 0.0398 ± 0.0018 and 0.2902 ± 0.0428, respectively. The apparent $^{206}Pb/^{238}U$ ages range from 230.9 to 304.5 Ma, with the majority of data points having a $^{206}Pb/^{238}U$ age of ~250 Ma, which is consistent with the age reported by Feng *et al.* (2021).

Alpha-decay dose and displacement per atom calculations

Alpha-decay dose (D) and displacement per atom (dpa) are two important parameters used to characterise the degree of metamictisation of columbite (Lumpkin and Ewing, 1988; Murakami *et al.*, 1991; Davis and Krogh, 2000; Lumpkin *et al.*, 2012; Feng *et al.*, 2020). The alpha-decay dose (D) can be calculated using the equation defined by Holland and Gottfried (1955), Lumpkin and Ewing (1988), and Lumpkin *et al.* (2012):

$$D = 8N_{238}(e^{t/\tau_{238}} - 1) + 7N_{235}(e^{t/\tau_{235}} - 1) + 6N_{232}(e^{t/\tau_{232}} - 1) \quad (1)$$

where D is the α-decay dose in α-events/mg, N_{238}, N_{235} and N_{232} are the number of atoms of ^{238}U, ^{235}U (equal to $^{238}U/137.88$) and ^{232}Th in 1 mg of columbite, respectively, and τ_{238}, τ_{235} and τ_{232} are the mean lives (equal to $1/\lambda$) of ^{238}U, ^{235}U and ^{232}Th, respectively. The age (t in Ma) utilised here is based on the U–Pb geochronological results. In per α-decay event, ~1500 displaced atoms are produced and the corresponding dpa values are calculated using the following formula (Matzke, 1982; Weber *et al.*, 1982; Weber and Roberts, 1983; Van Konynenburg and Guinan, 1983; Vance *et al.*, 1984; Eyal and Fleischer, 1985; Lumpkin and Ewing, 1988; Feng *et al.*, 2020):

$$dpa = 1500DM/(N_f N_A) \quad (2)$$

where D is the α-decay dose obtained from equation 1, M is the molecular weight (in mg) calculated using the EPMA data, and N_f and N_A are the number of atoms per formula unit and Avogadro's number, respectively. Metamictisation of minerals represents the combined effects of radiation damage accumulation and annealing (Nasdala *et al.*, 2001a, 2001b). Therefore, the annealing rate needs to be considered to correct the α-decay dose of columbite. Alpha-decay dose can be corrected for the effects of annealing using the average lifetime (200 Ma) of α-recoil trajectories of columbite (Lumpkin, 1992, 1998; Feng *et al.*, 2020). The correction is done as follows:

$$\begin{aligned} {}^{a}D = {} & 8N_{238}\left(\frac{\tau_a}{\tau_a + \tau_{238}}\right)[1 - (e^{t/\tau_{238} - t/\tau_a})] \\ & + 7N_{235}\left(\frac{\tau_a}{\tau_a + \tau_{235}}\right)[1 - (e^{t/\tau_{235} - t/\tau_a})] \\ & + 6N_{232}\left(\frac{\tau_a}{\tau_a + \tau_{232}}\right)[1 - (e^{t/\tau_{232} - t/\tau_a})] \end{aligned} \quad (3)$$

$$^{a}dpa = 1500{}^{a}DM/(N_f N_A) \quad (4)$$

The degrees of metamictisation for samples JR-1, DKLS 107, DKLS 108, K802 and K803 were calculated using equations 3 and 4. Some

Table 1. Major-element content of columbite in sample K650.*

	Core		Mantle		Rim	
	Average (n = 2)	S.D.	Average (n = 5)	S.D.	Average (n = 21)	S.D.
SiO_2	1.81	0.07	1.69	0.05	1.57	0.16
TiO_2	0.22	0.09	0.19	0.03	0.40	0.12
Al_2O_3	0.03	n.d.	0.02	0.02	0.03	0.01
$FeO_{tot.}$	0.16	0.09	0.14	0.08	0.19	0.06
MnO	18.25	0.48	18.58	0.17	18.70	0.23
MgO	n.d.	n.d.	n.d.	n.d.	0.01	0.00
CaO	0.04	0.01	0.04	0.01	0.03	0.01
Ta_2O_5	39.72	1.06	37.22	1.63	35.35	2.47
Nb_2O_5	37.40	2.57	40.72	2.14	42.00	2.38
SnO_2	0.01	n.d.	0.01	n.d.	0.02	0.01
Sc_2O_3	0.44	0.02	0.42	0.08	0.40	0.05
WO_3	0.37	0.03	0.48	0.15	0.65	0.19
Total	98.46	1.66	99.52	0.79	99.35	0.72
Atoms per formula unit on the basis of 6 O						
Si	0.121	0.008	0.110	0.005	0.102	0.011
Ti	0.011	0.005	0.009	0.001	0.020	0.006
Al	0.001	0.002	0.002	0.002	0.002	0.001
Fe	0.009	0.005	0.008	0.004	0.010	0.003
Mn	1.033	0.003	1.028	0.014	1.029	0.014
Mg					0.001	0.000
Ca	0.003	0.001	0.003	0.001	0.002	0.001
Ta	0.723	0.036	0.661	0.037	0.624	0.050
Nb	1.130	0.051	1.202	0.046	1.233	0.057
Sn	0.000		0.000		0.000	0.000
Sc	0.025	0.002	0.024	0.005	0.022	0.003
W	0.006	0.001	0.008	0.002	0.011	0.003
Total	3.063	0.006	3.055	0.009	3.057	0.009
Nb/Ta	1.567	0.149	1.819	0.182	1.991	0.242
#Mn	0.991	0.005	0.993	0.004	0.990	0.003
#Ta	0.390	0.023	0.355	0.022	0.337	0.028

*Notes: n.d. = not detected; S.D. = standard deviation; #Mn = molar Mn/(Mn + Fe) and #Ta =molar Ta/(Nb + Ta).

https://doi.org/10.1180/mgm.2023.18 Published online by Cambridge University Press

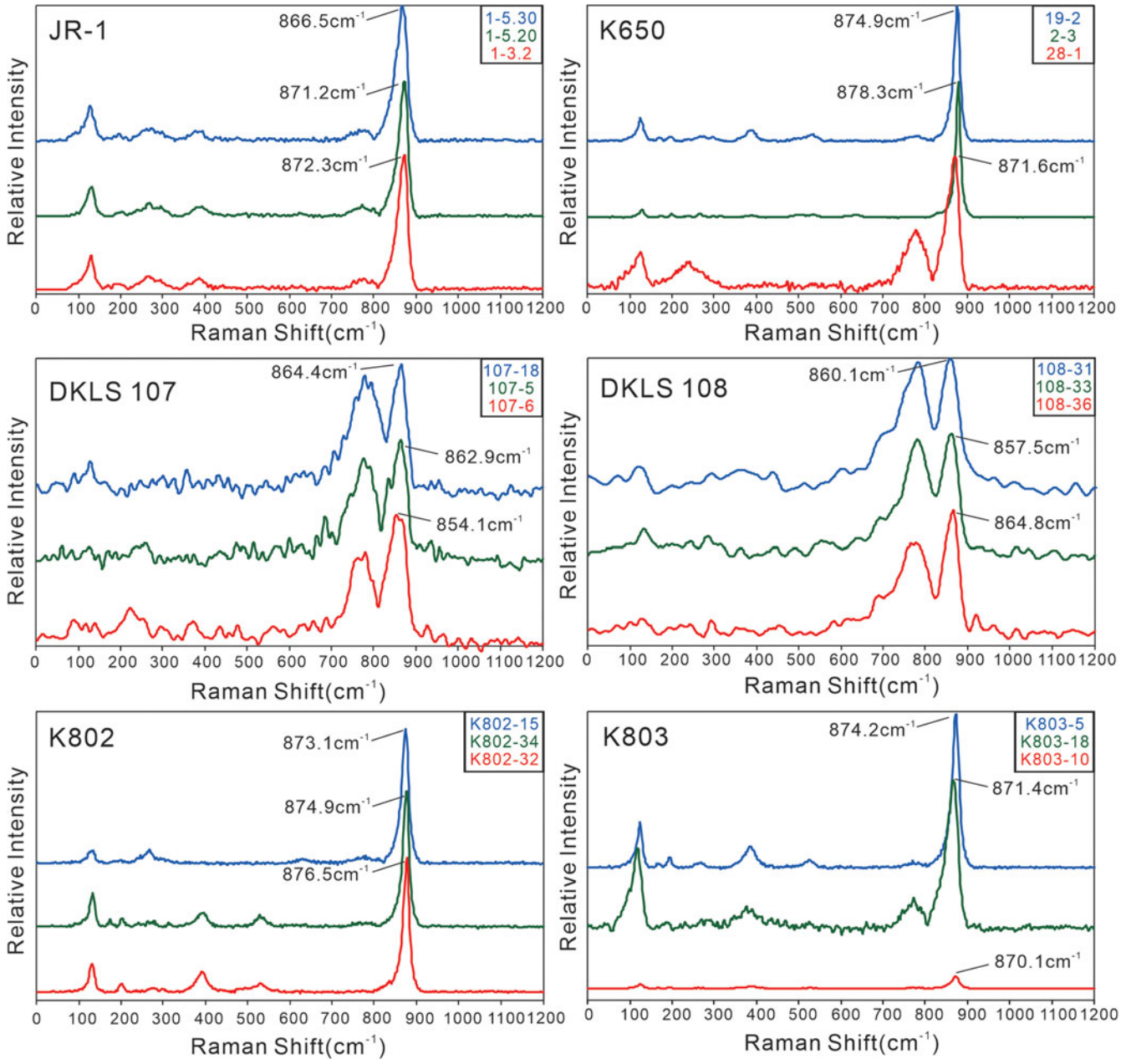

Figure 4. Representative Raman spectra for the columbite samples. All spectra show the strongest Raman band occurring at ~850–880 cm^{-1}.

of the U–Pb isotope ratios and trace-element concentrations required for the calculations of sample JR-1 are provided in Table 3. The full dataset is provided in Supplementary Table S1 and S4. The average degree of metamictisation calculated for each sample is provided in Table 4.

Feng *et al.* (2020) demonstrated that the ^{a}D values of fully crystalline and fully metamict columbite are $<0.2 \times 10^{16}$ α-events/mg and $>1.0 \times 10^{16}$α-events/mg, respectively, with columbite in a transitional state having ^{a}D values between these. According to Table 4, columbite in samples JR-1, K802 and K803 have relatively high degrees of crystallinity and did not undergo metamictisation. Columbite in samples DKLS 107 and DKLS 108, however, are in a state transitional to fully crystalline and fully metamict.

Discussion

Factors influencing the position and FWHM of the strongest columbite Raman band

Composition

Moreira *et al.* (2010) demonstrated that the strongest Raman band of columbite occurs at ~882 cm^{-1} and was related to the symmetric stretching vibration (A_{1g}) of the BO_6 chemical bond. As there is a difference in bond length between Nb–O and Ta–O, the average bond length of B–O should be related to the amount of Nb and Ta in this site. Therefore, the contents of Nb and Ta in columbite probably influences the position of its strongest Raman band (Moreira *et al.*, 2010). In contrast, variation in the amount of Fe and Mn has no significant impact on the bond length of

https://doi.org/10.1180/mgm.2023.18 Published online by Cambridge University Press

Table 2. Representative positions and FWHM values of the characteristic Raman band of columbite (A_{1g} vibration mode related to the B–O bond) in each pegmatite.*

Sample	EPMA data source	Position	#Mn	#Ta	p (cm^{-1})	FWHM (cm^{-1})
JR-1	Feng *et al.* (2021)	JR-1-3.2	0.84	0.08	872.3	22.1
		JR-1-5.20	0.84	0.08	871.2	24.2
		JR-1-5.30	0.84	0.08	866.5	30.2
DKLS 107	Feng *et al.* (2020)	107-18	0.78	0.45	864.4	33.6
		107-5	0.80	0.45	862.9	40.0
		107-6	0.80	0.45	854.1	54.1
DKLS 108	Feng *et al.* (2020)	108-36	0.72	0.18	864.8	32.7
		108-33	0.73	0.19	860.1	42.1
		108-31	0.73	0.18	857.5	50.7
K802	Feng *et al.* (2019)	K802-32	0.94	0.14	876.5	13.4
		K802-34	0.94	0.14	874.9	16.8
		K802-15	0.94	0.14	873.1	20.4
K803	Feng *et al.* (2019)	K803-5	0.94	0.18	874.2	18.2
		K803-18	0.94	0.18	871.4	23.3
		K803-10	0.91	0.18	870.1	26.3
K650	This study	K650-2-3	0.99	0.36	878.3	13.2
		K650-19-2	0.99	0.36	874.9	16.8
		K650-28-1	0.99	0.39	871.6	23.2

*Notes: #Mn = molar Mn/(Mn + Fe) and #Ta = molar Ta/(Nb + Ta); p = band position.

the B–O chemical bond in columbite (Tarantino and Zema, 2005), and should have no effect on the position and FWHM of its strongest Raman band (Moreira *et al.*, 2010). There are no significant variations in the Fe and Mn contents of columbite grains in samples K802, K803 and K650, however there are significant variations in their Nb and Ta contents (Table 2). The Raman spectra of columbite in samples K802, K803 and K650, which were acquired in the same locations as the EPMA, demonstrate that the positions of the strongest Raman bands occur within a narrow range of wavenumbers of 870.1–878.3 cm^{-1} and FWHM values of 13.2–26.3 cm^{-1}. Additionally, no correlation exists between band position, FWHM values, and Nb/Ta ratio of columbite (Table 4). Therefore, the Nb and Ta contents of columbite do not significantly influence the position and FWHM value of the strongest Raman band of columbite in the samples studied here.

Crystal orientation

Moreira *et al.* (2010) determined the Raman spectra of the same columbite-(Mn) crystal at different orientations. Their results demonstrated that the strongest band (A_{1g} vibration mode) was always present at ~882 cm^{-1}, but the FWHM value varied over a narrow range of 12–19 cm^{-1}. Different A_{1g}, B_{1g}, B_{2g} and B_{3g} vibration modes were recognised in the Raman spectra, however, when a, b and c were parallel or perpendicular to the polarisation direction of the incident laser. This indicates that changing the orientation of columbite crystals has only a limited effect on the position and FWHM value of the strongest band. In this study, crystal orientations were obtained on columbite crystals in samples JR-1 and DKLS 108 using EBSD (see Fig. 1 and Fig. 3). Raman spectra were obtained when the c axes of the crystals were parallel and perpendicular to the vibration direction of the excitation laser; the results are illustrated in Fig. 6. For sample JR-1, when the c axis is perpendicular to the vibration direction of the excitation laser, the position of the strongest band is 872–876 cm^{-1} and the FWHM value is 17–24 cm^{-1}. When the c axis is parallel to the vibration direction of the excitation laser, the position (868–869 cm^{-1}) and FWHM (24–25 cm^{-1}) of the strongest band are similar. For sample DKLS 108, when the c axis is perpendicular to the vibration direction of the excitation laser, the position of the strongest band is 862–864 cm^{-1} and the FWHM value is 31–34 cm^{-1}. When the c axis is parallel to the vibration direction of the excitation laser, the position (861–866 cm^{-1}) and FWHM (27–33 cm^{-1}) of the strongest Raman band are, again, similar, indicating that crystal orientation has limited effect on the position and FWHM values of the strongest Raman band of columbite.

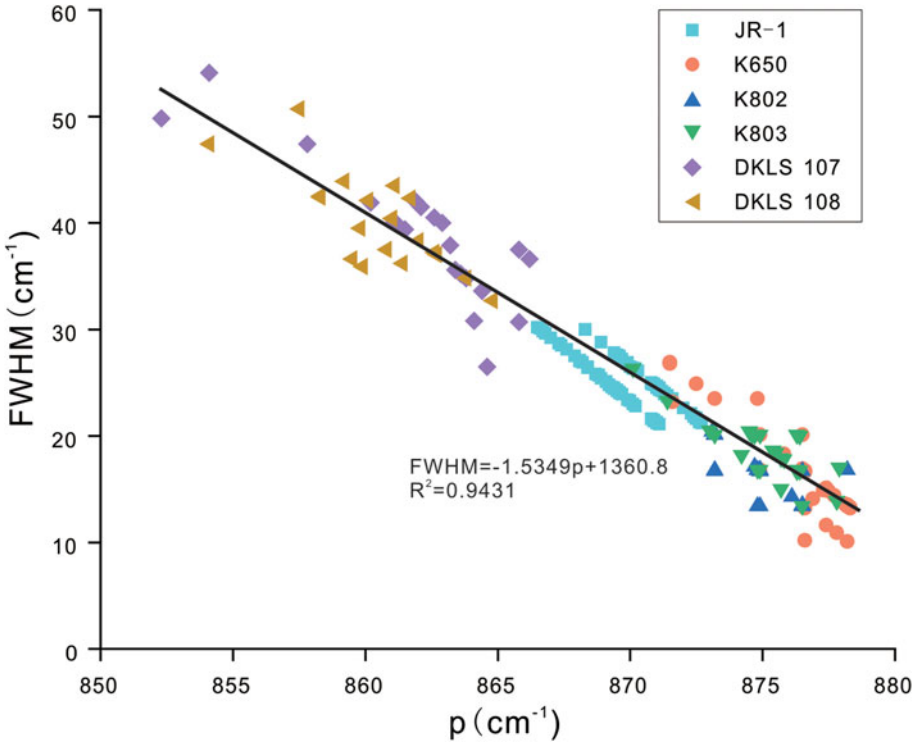

Figure 5. Bivariate diagram illustrating the correlation between the position and FWHM of the characteristic Raman band for columbite (A_{1g} vibration mode related to B–O bond) from all of the pegmatite samples.

https://doi.org/10.1180/mgm.2023.18 Published online by Cambridge University Press

Table 3. U–Pb geochronological results for sample JR-1 obtained using LA–ICP–MS.

			Isotopic ratios						Age(Ma)						
Position	U (ppm)	Th (ppm)	$^{207}Pb/^{206}Pb$	2σ	$^{207}Pb/^{235}U$	2σ	$^{206}Pb/^{238}U$	2σ	$^{207}Pb/^{235}U$	2σ	$^{206}Pb/^{238}U$	2σ	$^{207}Pb/^{206}Pb$	2σ	Concordance
JR-1-1.4	1694	17.3	0.0504	0.0016	0.2970	0.0120	0.0401	0.0013	263.9	9.1	253.5	8.1	211.0	71.0	95.9%
JR-1-1.6	1753	18.6	0.0506	0.0014	0.2870	0.0120	0.0404	0.0010	255.6	9.9	255.3	6.0	228.0	64.0	99.9%
JR-1-1.7	1760	20.9	0.0506	0.0011	0.2826	0.0082	0.0397	0.0010	252.4	6.5	250.8	6.3	222.0	53.0	99.4%
JR-1-1.8	1557	17.3	0.0517	0.0015	0.2892	0.0079	0.0401	0.0007	257.7	6.2	253.5	4.1	256.0	64.0	98.3%
JR-1-1.9	1426	15.0	0.0512	0.0012	0.2737	0.0070	0.0394	0.0006	246.0	5.7	249.1	3.8	240.0	54.0	98.8%
JR-1-1.10	1387	15.0	0.0502	0.0010	0.2700	0.0067	0.0394	0.0006	242.3	5.3	249.0	3.6	199.0	45.0	97.3%
JR-1-2.2	1595	23.0	0.0637	0.0019	0.3720	0.0110	0.0423	0.0006	323.2	8.4	266.8	4.0	738.0	61.0	78.9%
JR-1-2.3	1838	43.4	0.0778	0.0017	0.5240	0.0150	0.0484	0.0012	427.0	10.0	304.5	7.5	1140.0	46.0	59.8%
JR-1-2.6	1393	21.5	0.0523	0.0017	0.2820	0.0120	0.0401	0.0011	251.5	9.2	253.7	6.8	310.0	74.0	99.1%
JR-1-2.6.1	1603	16.3	0.0510	0.0014	0.2762	0.0070	0.0390	0.0006	247.4	5.6	246.4	3.4	224.0	59.0	99.6%
JR-1-2.7	1412	14.7	0.0508	0.0018	0.2810	0.0100	0.0394	0.0008	250.9	8.3	249.0	5.0	230.0	82.0	99.2%
JR-1-2.8	1722	29.3	0.0550	0.0014	0.3240	0.0100	0.0422	0.0011	285.6	7.8	266.2	7.1	419.0	58.0	92.7%
JR-1-2.9	1377	17.5	0.0514	0.0012	0.2781	0.0081	0.0393	0.0008	249.3	6.6	248.2	4.8	257.0	52.0	99.6%
JR-1-2.10	1526	15.4	0.0495	0.0012	0.2719	0.0074	0.0398	0.0005	243.9	5.9	251.7	3.0	173.0	55.0	96.9%
JR-1-3.1	1666	18.7	0.0496	0.0013	0.2639	0.0066	0.0381	0.0007	237.6	5.3	241.1	4.2	165.0	60.0	98.5%
JR-1-3.2	1344	17.0	0.0538	0.0014	0.2940	0.0100	0.0394	0.0008	261.3	7.9	249.2	4.9	343.0	59.0	95.1%
JR-1-3.3	1690	18.6	0.0524	0.0013	0.2649	0.0072	0.0365	0.0006	238.3	5.8	230.9	3.7	298.0	56.0	96.8%
JR-1-3.5	711	9.8	0.0528	0.0041	0.3080	0.0220	0.0409	0.0012	272.0	17.0	258.6	7.6	380.0	170.0	94.8%
JR-1-3.8	1039	15.4	0.0517	0.0015	0.2855	0.0098	0.0399	0.0008	254.3	7.7	251.9	5.1	264.0	60.0	99.0%
JR-1-3.9	1039	13.2	0.0522	0.0015	0.2832	0.0093	0.0393	0.0006	253.4	7.2	248.6	3.6	286.0	63.0	98.1%
JR-1-3.10	1026	12.2	0.0525	0.0014	0.2809	0.0085	0.0392	0.0007	251.4	6.9	248.1	4.2	293.0	62.0	98.7%
JR-1-4.1	1228	14.2	0.0531	0.0031	0.2950	0.0180	0.0399	0.0012	261.0	14.0	252.5	7.2	330.0	140.0	96.6%
JR-1-4.5	1821	19.0	0.0537	0.0025	0.2960	0.0130	0.0398	0.0009	263.0	10.0	251.5	5.3	360.0	99.0	95.4%
JR-1-4.6	1737	18.2	0.0534	0.0033	0.2860	0.0170	0.0397	0.0013	255.0	14.0	251.1	8.3	320.0	140.0	98.4%
JR-1-4.7	1680	18.4	0.0514	0.0022	0.2870	0.0120	0.0400	0.0010	255.6	9.3	252.7	6.4	240.0	94.0	98.9%
JR-1-4.8	1640	17.8	0.0516	0.0022	0.2890	0.0120	0.0404	0.0009	258.6	8.9	255.0	5.5	244.0	95.0	98.6%
JR-1-4.9	2080	22.5	0.0505	0.0022	0.2570	0.0110	0.0367	0.0008	232.4	9.0	232.1	5.2	206.0	99.0	99.9%
JR-1-4.10	1505	17.1	0.0498	0.0012	0.2681	0.0073	0.0394	0.0006	240.6	5.9	249.3	3.8	189.0	53.0	96.5%
JR-1-5.3	1674	17.9	0.0533	0.0020	0.2774	0.0096	0.0373	0.0006	248.5	7.7	236.0	3.5	334.0	84.0	94.7%
JR-1-5.6	1438	15.9	0.0514	0.0013	0.2787	0.0095	0.0391	0.0010	251.0	7.5	247.6	6.2	265.0	57.0	98.6%
JR-1-5.7	1316	14.2	0.0505	0.0020	0.2800	0.0120	0.0399	0.0014	250.6	9.2	252.1	8.5	219.0	88.0	99.4%
JR-1-5.8	1172	12.7	0.0505	0.0013	0.2735	0.0083	0.0392	0.0006	247.5	6.5	248.1	3.7	203.0	57.0	99.8%
JR-1-5.9	1246	13.3	0.0505	0.0010	0.2792	0.0066	0.0401	0.0008	250.2	5.3	253.2	4.7	208.0	43.0	98.8%
JR-1-5.10	1544	17.3	0.0509	0.0008	0.2782	0.0061	0.0405	0.0005	249.3	4.8	256.0	3.2	229.0	37.0	97.4%
JR-1-6.6	1169	13.4	0.0516	0.0012	0.2769	0.0068	0.0394	0.0006	248.6	5.5	248.8	3.8	253.0	51.0	99.9%
JR-1-6.7	1221	13.6	0.0507	0.0011	0.2748	0.0061	0.0395	0.0006	246.2	4.8	249.8	3.8	227.0	47.0	98.6%
JR-1-6.8	1219	13.5	0.0506	0.0010	0.2733	0.0059	0.0393	0.0005	245.5	4.7	248.2	2.9	223.0	43.0	98.9%
JR-1-6.9	1227	13.4	0.0513	0.0010	0.2797	0.0057	0.0392	0.0005	250.2	4.5	247.7	3.2	248.0	44.0	99.0%
JR-1-6.10	1243	13.9	0.0517	0.0010	0.2792	0.0067	0.0391	0.0006	250.1	5.4	247.3	3.9	268.0	44.0	98.9%

Radiation damage

Metamictisation of U- and Th-rich minerals is attributed to the destruction of the crystal lattice by radiation damage (mainly α-decay). When the cumulative radiation damage exceeds the self-healing rate of the mineral, metamictisation will occur (Ewing, 1975; Nasdala *et al.*, 2001a; Romer, 2003). Previous studies have shown that the band position and FWHM of the ($\upsilon_3(SiO_4)$) Raman band of zircon changes systematically with degree of metamictisation (Nasdala *et al.*, 1995; Zhang *et al.*, 2000; Balan *et al.*, 2001; Nasdala *et al.*, 2001b; Nasdala *et al.*, 2004; Nasdala *et al.*, 2005). Similarly, with increasing degree of metamictisation, the position of the strongest Raman band of columbite in each sample decreases gradually and the FWHM increases gradually (see Table 4). This indicates that radiation damage has a significant influence on the Raman characteristic band of columbite.

Table 4. Corrected α-decay doses, displacements per atom, and key parameters of the strongest Raman bands of the analysed columbite grains.*

Sample	^{a}D (× 10^{15})	S.D.	^{a}dpa	S.D.	*p* (cm^{-1})	S.D.	FWHM (cm^{-1})	S.D.
K802	0.169	0.077	0.017	0.008	874.9	1.2	16.6	1.9
K803	0.268	0.166	0.028	0.017	875.3	1.6	18.5	3.1
DKLS 107	3.119	0.371	0.355	0.042	862.1	3.5	38.8	6.4
DKLS 108	2.748	0.435	0.281	0.045	860.5	2.3	40.1	4.3
JR-1	0.638	0.115	0.066	0.006	869.9	1.5	25.1	2.4

*The unit for ^{a}D is α-events/mg; ^{a}dpa represents the amount of atomic displacement caused by each α decay; *p* – band position; S.D. – standard deviation.

Murakami *et al.* (1991) noted that the α-decay dose threshold for fully metamict zircon is 8.0×10^{15} α-events/mg. According to Feng *et al.* (2020), the α-decay dose threshold for fully metamict columbite is 1×10^{16} α-events/mg (after correcting for the effects of annealing), which is much larger than that of zircon. This indicates that columbite is probably more resistant to radiation damage than zircon in highly fractionated granites and granitic pegmatites. Therefore, the U–Pb age of columbite is more suitable than that of zircon to constrain the age of highly fractionated granites and granite pegmatites.

Correlation between position and FWHM of the strongest Raman band (A_{1g} vibration mode)

The position and FWHM values of the Raman characteristic band of the analysed columbites are correlated negatively (Fig. 5). This

https://doi.org/10.1180/mgm.2023.18 Published online by Cambridge University Press

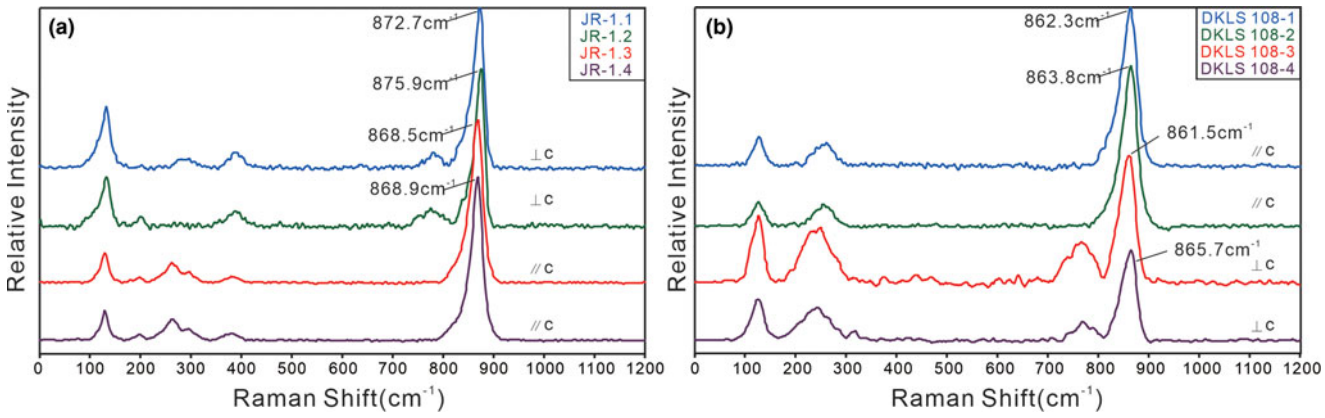

Figure 6. Raman spectra of columbite grains in samples: (a) JR-1; and (b) DKLS 108. Analyses JR-1.1 and JR-1.2 represent spectra of crystals where the c axis is perpendicular to the vibration direction of the excitation laser, whereas JR-1.3 and JR-1.4 represent spectra of crystals where the c axis is parallel to the vibration direction of the excitation laser. Analyses DKLS 108-1 and DKLS 108-2 represent spectra of crystals where the c axis is parallel to the vibration direction of the excitation laser, whereas DKLS 108-3 and DKLS 108-4 represent spectra of crystals where the c axis is perpendicular to the vibration direction of the excitation laser.

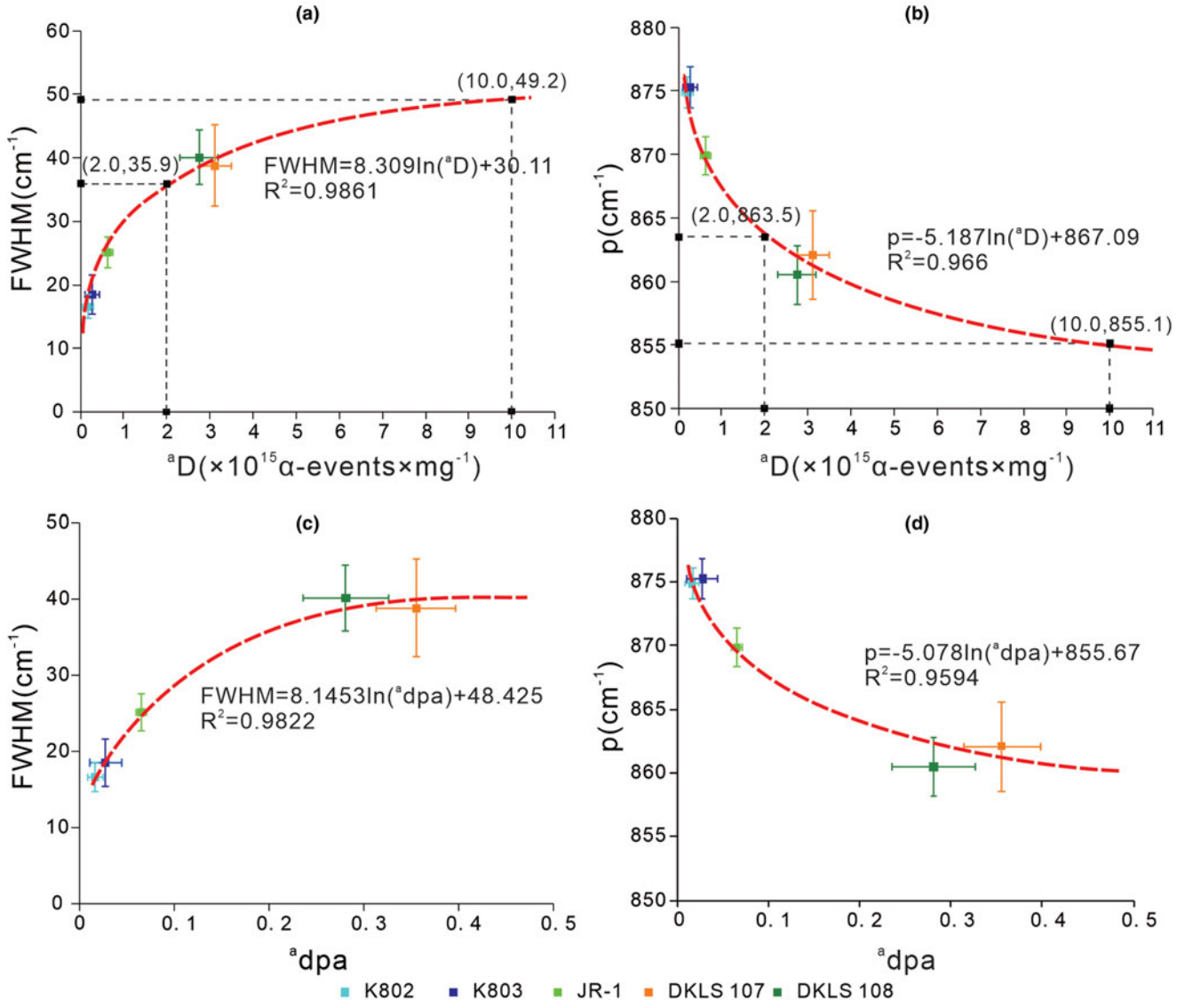

Figure 7. Bivariate diagrams illustrating the relationships between: (a) alpha-decay dose (^{a}D) *vs*. FWHM; (b) alpha-decay dose (^{a}D) *vs*. band position (*p*); (c) displacements per atom (^{a}dpa) *vs.* FWHM; and (d) displacements per atom (^{a}dpa) *vs.* band position (*p*) for the characteristic Raman band of columbite (A_{1g} vibration mode related to B–O bond) from all of the pegmatite samples.

https://doi.org/10.1180/mgm.2023.18 Published online by Cambridge University Press

negative correlation is evident in columbite-(Mn) grains collected from the same pegmatite, and also in those characterised by different degrees of metamictisation. From Table 4, we know that these samples have different degrees of metamictisation, however the positions of the Raman characteristic bands are all negatively correlated with FWHM values according to Fig. 5. The correlation between the two parameters can be quantified using the following equation ($R^2 = 0.9431$):

$$p = -1.5349\text{FWHM} + 1360.8 \quad (5)$$

This correlation equation can be used to quantitatively characterise the relationship between the position and FWHM of the strongest Raman band of columbite. This negative correlation among variably metamict columbite is similar to that for zircon that has undergone variable degrees of metamictisation (Nasdala *et al.*, 2005). This supports the suggestion that the variation in position of the characteristic Raman band of columbite is not controlled by its composition or crystal orientations, but rather is primarily controlled by its degree of metamictisation.

Quantifying the degree of metamictisation of columbite using Raman spectroscopy

The results that are summarised in Table 4 demonstrate that, with increasing degree of metamictisation, the position of the strongest Raman band of columbite shifts towards lower wavenumbers and its FWHM value increases. A relationship can, therefore, be established to characterise quantitatively the degree of metamictisation of columbite using the position and FWHM values of the strongest Raman band (Fig. 7), in a manner similar to that proposed for zircon (Nasdala *et al.*, 2005). In contrast to the relationship for zircon, however, our results suggest that band position and FWHM are related to degree of metamictisation of columbite via a logarithmic relationship (Fig. 7). For columbite, the quantitative relationship between α-decay dose ^{a}D ($\times 10^{15}$ α-events/mg) and the FWHM (cm^{-1}), displacements per atom (^{a}dpa) and the FWHM (cm^{-1}), α-decay dose ^{a}D ($\times 10^{15}$ α-events/mg) and the band position p (cm^{-1}), and displacements per atom (^{a}dpa) and the band position p (cm^{-1}) can be quantified, respectively, via following relationships:

$$\text{FWHM} = 8.309 \times \ln(^{a}D) + 30.11,\ R^2 = 0.9861; \quad (6)$$

$$\text{FWHM} = 8.1453 \times \ln(^{a}\text{dpa}) + 48.425,\ R^2 = 0.9822; \quad (7)$$

$$p = -5.187 \times \ln(^{a}D) + 867.09,\ R^2 = 0.966; \quad (8)$$

$$p = -5.078 \times \ln(^{a}\text{dpa}) + 855.67,\ R^2 = 0.9594. \quad (9)$$

On the basis of these relationships, once the FWHM value of the strongest band of columbite reaches ~50 cm^{-1} (Fig. 7), the crystal is likely to be completely metamict (the associated alpha-decay dose [^{a}D] corrected for annealing is 1.0×10^{16} α-events/mg) (Lumpkin, 1998; Feng *et al.*, 2020) and not be suitable for geochronological studies.

Conclusions

On the basis of systematic Raman spectroscopic analysis of columbite grains from six samples (JR-1, DKLS 107, DKLS 108, K802, K803 and K650) from five pegmatites (the Jing'erquan No. 1 spodumene pegmatite, the Dakalasu No. 1 pegmatite dyke, the No. 802 and No. 803 spodumene pegmatites, and the No. 650 pegmatite dyke of Kalu'an), the following conclusions can be drawn regarding controls on the parameters of their strongest Raman bands: (1) the main factor that influences the position and FWHM value of the Raman characteristic band (A_{1g} vibration mode related to B–O bond) of columbite-(Mn) is metamictisation caused by radiation damage; composition and crystal orientations have limited influence; (2) the position of the strongest Raman band of columbite is correlated negatively with FWHM values; and (3) with increasing degree of metamictisation, the band position of the characteristic Raman band shifts towards lower wavenumbers and the FWHM value systematically increases.

The results presented here demonstrate that the position and FWHM value of the characteristic Raman band for columbite can be used to quantitatively assess their degree of metamictisation.

Acknowledgements. This research was supported financially by The National Natural Science Foundation of China (grant No. 41902073 and 91962214), Department of Science and Technology of Shaanxi Province, China (grant No. 2020JM-215), and the Fundamental Research Funds for the Central Universities (grant No. 300102272504). The authors would like to thank Dr. Huan Hu at Nanjing University for their assistance with EPMA and LA–ICP–MS analyses. We appreciate the constructive comments from the two anonymous reviewers that greatly helped to improve the manuscript.

Supplementary material. The supplementary material for this article can be found at https://doi.org/10.1180/mgm.2023.18.

Competing interests. The authors declare none.

References

Balan E., Neuville D.R., Trocellier P., Fritsch E., Muller J.P. and Calas G. (2001) Metamictization and chemical durability of detrital zircon. *American Mineralogist*, **86**, 1025–1033.

Baumgartner R., Romer R.L., Moritz R., Sallet R. and Chiaradia M. (2006) Columbite-tantalite bearing granitic pegmatites from the Seridó Belt, northeastern Brazil: genetic constraints from U-Pb dating and Pb isotopes. *The Canadian Mineralogist*, **44**, 69–86.

Černý P. and Ercit T.S. (1989) Mineralogy of niobium and tantalum: crystal chemical relationships, paragenetic aspects and their economic implications. Pp. 27–79 in: *Lanthanides, Tantalum and Niobium* (Möller P., Černý P. and Saupé F., editors). Special Publication No. 7 of the Society for Geology Applied to Mineral Deposits, Springer, Berlin.

Che X.D., Wu F.Y., Wang R.C., Gerdes A., Ji W.Q., Zhao Z.H., Yang J.H. and Zhu Z.Y. (2015) In situ U-Pb isotopic dating of columbite-tantalite by LA-ICP-MS. *Ore Geology Reviews*, **65**, 979–989.

Davis D.W. and Krogh T.E. (2000) Preferential dissolution of ^{234}U and radiogenic Pb from α-recoil-damaged lattice sites in zircon: implications for thermal histories and Pb isotopic fractionation in the near surface environment. *Chemical Geology*, **172**, 41–58.

Deng X.D., Li J.W., Zhao X.F., Hu Z.C., Hu H., Selby D. and Souza Z.S.D. (2013) U-Pb isotope and trace element analysis of columbite-(Mn) and zircon by laser ablation ICP-MS: implications for geochronology of pegmatite and associated ore deposits. *Chemical Geology*, **344**, 1–11.

Ercit T.S. (1994) The geochemistry and crystal chemistry of columbite-group minerals from granitic pegmatites, southwestern Grenville Province, Canadian Shield. *The Canadian Mineralogist*, **32**, 421–438.

Ewing R.C. (1975) The crystal chemistry of complex niobium and tantalum oxides. IV. The metamict state: Discussion. *American Mineralogist*, **60**, 728–733.

Eyal Y. and Fleischer R.L. (1985) Preferential leaching and the age of radiation damage from alpha decay in minerals. *Geochimica et Cosmochimica Acta*, **49**, 1155–1164.

Feng Y.G., Liang T., Zhang Z., Wang Y.Q., Zhou Y., Yang X.Q., Gao J.G., Wang H. and Ding K. (2019) Columbite U-Pb geochronology of Kalu'an

lithium pegmatites in Northern Xinjiang, China: Implications for genesis and emplacement history of rare-element pegmatites. *Minerals*, **9**, 456.

Feng Y.G., Liang T., Linnen R., Zhang Z., Zhou Y., Zhang Z.L., and Gao J.G. (2020) LA-ICP-MS dating of high uranium columbite from no. 1 pegmatite at Dakalasu, the Chinese Altay orogen: Assessing effect of metamictization on age concordance. *Lithos*, **362–363**, 105461.

Feng Y.G., Liang T., Lei R.X., Ju M.H., Zhang Z.L., Gao J.G., Zhou Y. and Wu C.Z. (2021) Relationship between undercooling and emplacement of rare-element pegmatites-thinking based on field observations and pegmatite geochronology. *Journal of Earth Sciences and Environment*, **43**, 100–116.

Hellstrom J., Paton C., Woodhead J. and Hergt J. (2008) Iolite: Software for spatially resolved LA-(quad and MC) -ICP-MS analysis. Pp. 343–348 in: *Laser Ablation ICP-MS in the Earth Sciences: Current Practices and Outstanding Issues* (P. Sylvestor, editors). Mineralogical Association of Canada, Quebec, Canada.

Holland H.D. and Gottfried D. (1955) The effect of nuclear radiation on the structure of zircon. *Acta Crystallographica*, **8**, 291–300.

Husson E., Repelin Y., Dao N.Q. and Brusset H. (1977) Characterization of different bondings in some divalent metal niobates of columbite structure. *Materials Research Bulletin*, **12**, 1199–1206.

Linnen R.L., Van Lichtervelde M. and Černý P. (2012) Granitic pegmatites: granitic pegmatites as sources of strategic metals. *Elements*, **8**, 275–280.

Liu S.Y., Wang R., Jeon H., Hou Z.Q., Xue Q.W., Zhou L.M., Chen S.B., Zhang Z.L. and Xi B.B. (2020) Indosinian magmatism and rare metal mineralization in East Tianshan orogenic belt: An example study of Jingerquan Li-Be-Nb-Ta pegmatite deposit. *Ore Geology Reviews*, **116**, 103265.

Ludwig K.R. (2003) *User's Manual for a Geochronological Toolkit for Microsoft Excel (Isoplot/Ex version 3.0)*. Special Publication 4. Berkeley Geochronology Center, Berkely, California, USA, pp. 70.

Lumpkin G.R. (1992) Analytical electron microscopy of columbite: A niobium-tantalum oxide mineral with zonal uranium distribution. *Journal of Nuclear Materials*, **190**, 302–311.

Lumpkin G.R. (1998) Composition and structural state of columbite-tantalite from the Harding Pegmatite, Taos County, New Mexico. *The Canadian Mineralogist*, **36**, 585–599.

Lumpkin G.R. and Ewing R.C. (1988) Alpha-decay damage in minerals of the pyrochlore group. *Physics and Chemistry of Minerals*, **16**, 2–20.

Lumpkin G.R., Leung S.H.F. and Ferenczy J. (2012) Chemistry, microstructure, and alpha decay damage of natural brannerite. *Chemical Geology*, **291**, 55–68.

Lupulescu M.V., Chiarenzelli J.R., Pecha M.E., Singer J.W. and Regan S.P. (2018) Columbite-group minerals from New York pegmatites: Insights from isotopic and geochemical analyses. *Geosciences*, **8**, 169.

Ma Z.L., Zhang H., Tang Y., Lv Z.H., Zhang X. and Zhao J.Y. (2015) Zircon U-Pb geochronology and Hf isotopes of pegmatites from the Kaluan mining area in the Altay, Xinjiang and their genetic relationship with the Halong granite. *Geochimica*, **44**, 9–26.

Matzke Hj. (1982) Radiation damage in crystalline insulators, oxides and ceramic nuclear fuels. *Radiation Effects*, **64**, 3–33.

Melcher F., Graupner T., Gäbler H.E., Sitnikova M. and Dewaele S. (2015) Tantalum-(niobium-tin) mineralisation in African pegmatites and rare metal granites: Constraints from Ta-Nb oxide mineralogy, geochemistry and U-Pb geochronology. *Ore Geology Reviews*, **64**, 667–719.

Melcher F., Graupner T., Gäbler H.E., Sitnikova M., Oberthür T., Gerdes A., Badanina E. and Chudy T. (2017) Mineralogical and chemical evolution of tantalum-(niobium-tin) mineralisation in pegmatites and granites. Part 2: Worldwide examples (excluding Africa) and an overview of global metallogenetic patterns. *Ore Geology Reviews*, **89**, 946–987.

Melleton J., Gloaguen E., Frei D., Novák M. and Breiter K. (2012) How are the emplacement of rare-element pegmatites, regional metamorphism and magmatism interrelated in the Moldanubian Domain of the Variscan Bohemian Massif, Czech Republic? *The Canadian Mineralogist*, **50**, 1751–1773.

Moreira R.L., Rubinger C.P., Krambrock K. and Dias A. (2010) Polarized Raman scattering and infrared spectroscopy of a natural manganocolumbite single crystal. *Raman Spectroscopy*, **41**, 1044–1049.

Murakami T., Chakoumakos B.C., Ewing R.C., Lumpkin G.R. and Weber W.J. (1991) Alpha-decay event damage in zircon. *American Mineralogist*, **76**, 1510–1532.

Nasdala L., Irmer G. and Wolf D. (1995) The degree of metamictization in zircons: a Raman spectroscopic study. *European Journal of Mineralogy*, **7**, 471–478.

Nasdala L., Wenzel M., Vavra G., Irmer G., Wenzel T. and Kober B. (2001a) Metamictisation of natural zircon: accumulation versus thermal annealing of radioactivity-induced damage. *Contributions to Mineralogy and Petrology*, **141**, 125–144.

Nasdala L., Beran A., Libowitzky E. and Wolf D. (2001b) The incorporation of hydroxyl groups and molecular water in natural zircon ($ZrSiO_4$). *American Journal of Science*, **301**, 831–857.

Nasdala L., Smith D.C., Kaindl R. and Zieman M.A. (2004) Raman spectroscopy: Analytical perspectives in mineralogical research. *EMU Notes in Mineralogy*, **6**, 281–343.

Nasdala L., Hanchar J.M., Kronz A. and Whitehouse M.J. (2005) Long-term stability of alpha particle damage in natural zircon. *Chemical Geology*, **220**, 83–103.

Romer R.L. (2003) Alpha-recoil in U-Pb geochronology: effective sample size matters. *Contributions to Mineralogy and Petrology*, **145**, 481–491.

Romer R.L. and Smeds S.A. (1994) Implications of U-Pb ages of columbite-tantalites from granitic pegmatites for the Palaeoproterozoic accretion of 1.90–1.85 Ga magmatic arcs to the Baltic Shield. *Precambrian Research*, **67**, 141–58.

Romer R.L., Smeds S.A. and Ern P. (1996) Crystal-chemical and genetic controls of U–Pb systematics of columbite-tantalite. *Mineralogy and Petrology*, **57**, 243–260.

Smith S.R., Foster G.L., Romer R.L., Tindle A.G., Kelley S.P., Noble S.R., Horstood M. and Breaks F.W. (2004) U-Pb columbite-tantalite chronology of rare-element pegmatites using TIMS and Laser Ablation-Multi Collector-ICP-MS. *Contributions to Mineralogy and Petrology*, **147**, 549–564.

Tarantino S.C. and Zema M. (2005) Mixing and ordering behavior in manganocolumbite-ferrocolumbite solid solution: A single-crystal X-ray diffraction study. *American Mineralogist*, **90**, 1291–1300.

Váczi and Tamás. (2014) A new, simple approximation for the deconvolution of instrumental broadening in spectroscopic band profiles. *Applied Spectroscopy*, **68**, 1274–1278.

Vance E.R., Kariorsis F.G., Cartz L. and Wong M.S. (1984) Radiation effects on sphene and sphene-based glass ceramics. Pp. 62–67 in: *Advances in Ceramics, Vol 8* (G.G. Wicks and W.A. Ross, editors). American Ceramic Society, Columbus, USA.

Van Konynenburg R.A. and Guinan M.W. (1983) Radiation effects in SYNROC-D. *Nuclear Technology*, **60**, 206–217.

Wang D.H., Chen Y.C. and Xu Z.G. (2003) $^{40}Ar/^{39}Ar$ isotope dating on muscovites from Indosinian rare metal deposits in Central Altay Northwestern China. *Bulletin of Mineralogy Petrology and Geochemistry*, **22**, 14–17.

Weber W.J. and Roberts F.P. (1983) A review of radiation effects in solid nuclear waste forms. *Nuclear Technology*, **60**, 178–198.

Weber W.J., Turcotte R.P. and Roberts F.P. (1982) Radiation damage from alpha decay in ceramic nuclear waste forms. *Waste Management*, **2**, 295–319.

Yan Q.H., Qiu Z.W., Wang H., Wang M., Wei X.P., Li P., Zhang R.Q., Li C.Y. and Liu J.P. (2018) Age of the Dahongliutan rare metal pegmatite deposit, West Kunlun, Xinjiang (NW China): Constraints from LA-ICP-MS U-Pb dating of columbite-(Fe) and cassiterite. *Ore Geology Reviews*, **100**, 561–573.

Yao F.J., Xu X.W., Yang J.M., Wu L.N. and Geng X.X. (2020) A technology for identifying Li-Be pegmatite using ASTER remote sensing data in granite of Gobi shallow-covered area: A case study of recognition and prediction of Li-Be pegmatite in Jingerquan, Xinjiang. *Mineral Deposits*, **39**, 686–696 [in Chinese with English abstract].

Zhang M., Salje E.K.H., Farnan I., Graeme-Barber A., Daniel P., Ewing R.C., Clark A.M. and Leroux H. (2000) Metamictization of zircon: Raman spectroscopic study. *Journal of Physics: Condensed Matter*, **12**, 1915–1925.

Zhou Q.F., Qin K.Z., Tang D.M., Wang C.L. and Sakyi P.A. (2018) LA-ICP-MS U-Pb zircon, columbite-tantalite and $^{40}Ar–3^{9}Ar$ muscovite age constraints for the rare-element pegmatite dykes in the Altai orogenic belt, NW China. *Geological Magazine*, **155**, 707–728.

Zou T.R. and Li Q.C. (2006) *Rare and Rare Earth Metallic Deposits in Xinjiang, China*. Geological Publishing House, Beijing, 284 pp [in Chinese with English abstract].

https://doi.org/10.1180/mgm.2023.18 Published online by Cambridge University Press